Ocean Engineering
April 2022, Volume 250 Pages 110921 (11p.)
https://doi.org/10.1016/j.oceaneng.2022.110921
https://archimer.ifremer.fr/doc/00755/86694/

Archimer
https://archimer.ifremer.fr

An experimental blade-controlled platform for the design of smart cross-flow propeller

Fasse Guillaume [1, *], Becker Florent [1], Hauville Frederic [1], Astolfi Jacques-Andre [1], Germain Gregory [2]

[1] Naval Academy Research Institute, BCRM Brest, CC600, 29240 Brest Cedex9, France
[2] Ifremer, Marine Structure Laboratory, Boulogne-sur-Mer, 62200, France

* Corresponding author : Guillaume Fasse, email address : guillaume.fasse@ecole-navale.fr

Abstract :

As an academic platform, the French Naval Academy Research Institute (IRENav) developed a large-scale experimental cycloidal propeller (800 kg, 0.4 m radius) with the aim of running diverse pitch motions to evaluate performances of cross-flow propellers. Blades' pitching is here performed by servo-motors in order to control each blade independently. Blade pitch regulation has been improved to obtain a quick response of auxiliary servo-motors. However, pitch tracking validation shows a systemic error due the PI regulation loop which depends on the rotational speed and the considered pitch law (the sharper the law, the higher the error). The platform is widely instrumented with load and torque sensors to measure inflow hydrodynamic forces during the rotation. First experiments have been performed at the IFREMER wave–current flume tank for a range of sinusoidal pitch laws to confirm the post process procedure and to determine performances for a range of advance parameters. Results show that depending on the advance parameter the more different efficient law is: the higher the advance parameter, the lower the sinusoidal amplitude must be for a better efficiency. These results confirm the requirement of an adaptable pitch control for cycloidal propeller to boost their performances.

Keywords : Cycloidal propulsion, Experimental test-bench, Blade-control

Please note that this is an author-produced PDF of an article accepted for publication following peer review. The definitive publisher-authenticated version is available on the publisher Web site.

1. Introduction

For the last two decades, innovative naval propulsion systems have been investigated thanks to the growing development of unmanned underwater vehicles. Cross-flow propellers are promising alternative concepts to the usual screw propellers. These systems use mechanical energy from unsteady hydrodynamic forces generated by blades oscillation or heaving like natural marine animal swimmers, referred as bio-mimetism (Barrett et al., 1999; Sparenberg, 2002; Triantafyllou et al., 2004).

Cross-flow propellers are characterized by the rotation of several blades around a main axis which is perpendicular to the freestream, as opposed to the conventional screw propeller whose rotation axis is usually aligned with the freestream. The main rotation is associated with the oscillation of each blade around its own axis commonly called pitch rotation. The combination of these two rotations produces an unsteady hydrodynamic load which results in the thrust force (in the ship advance direction) and side force (perpendicular to the advance direction). Theses forces vary along the main rotation angle, called orbital position θ, and depend highly on the running pitch law.

The main advantage of these propellers is to generate a 360° vectorial thrust force that significantly improves the ship's maneuverability. For this kind of propulsion, the advance parameter λ is defined as the ratio of the ship's advance speed V_a to the rotational tip speed $V_r = \Omega R$ (where R is the vertical axis propeller radius):

$$\lambda = \frac{V_a}{V_r} \tag{1}$$

Depending on its value two modes are distinguished by the blade kinematic which describes a cycloid path (cross-flow propeller is also referred as cycloidal propeller). Epicycloidal mode is defined for $\lambda < 1$: the rotational tip speed is higher than the ship's advance speed (see Figure 1). The blade leading edge is hence mainly parallel to the tangent of the rotational tip speed to ensure that the relative kinematic velocity (vectorial sum of V_a and V_r) is coming from the leading edge (and not from the trailing edge). Propellers using this kinematic mode are referred to as low-pitch systems.

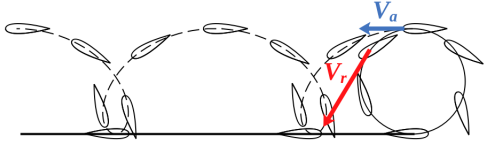

Figure 1: Illustration of the epicycloidal path of one blade

On the other hand, trochoidal mode for $\lambda > 1$ allows the decrease of the rotational speed in comparison with the epicycloidal mode for the same advance speed. Because the advance speed is predominant in the expression of the kinematic relative velocity, the blade's leading edge is roughly aligned with the advance direction (see Figure 2). Decreasing the rotational speed has the main benefit of delaying the blades' cavitation. These propellers are referred to as high-pitch systems.

*Corresponding author
guillaume.fasse@ecole-navale.fr (G. Fasse)
ORCID(s): 0000-0002-1256-0561 (G. Fasse)

List of Abbreviations

CAN	Controller Area Network
CHI	Computer Human Interface
FPGA	Field-Programmable Gate Array
MCU	Micro Controller Unit
MP	Primary Motor
MSi	Secondary Motors i
PID	Proportional Integral Derivative
PMSM	Permanent Magnet Synchronous Machine
PWD	Pulse Width Modulation
RT	Real Time

Nomenclature

α	Angle of attack $[deg]$
β	Blade pitch angle defined between the ortho-radial tangent and the blade chord $[deg]$
$\beta_{ref}(\theta)$	Pitch law reference $[deg]$
λ	Advance parameter
ν	Kinematic viscosity $[m^2.s^{-1}]$
Ω	Main rotational speed $[RPM]$
σ	Solidity of the cross-flow propeller
θ	Orbital position $[deg]$
φ	Blade pitch angle defined between the ship advance speed and blade chord $[deg]$
AR	Aspect ratio of the blade
c	Blade chord $[m]$
C_{F_N}	Normal force coefficient
C_{F_T}	Tangential force coefficient
C_{F_X}	Thrust force coefficient
C_{F_Y}	Side force coefficient
c_r	Blade chord ratio
C_T	Torque coefficient
D	Cross-flow propeller diameter $[m]$
F_{Nb}	Blade hydrodynamic force along the blade-normal direction $[N]$
F_N	Blade hydrodynamic force along the rotor-normal direction $[N]$
F_{Tb}	Blade hydrodynamic force along the blade-tangential direction $[N]$
F_T	Blade hydrodynamic force along the rotor-tangential direction $[N]$
F_X	Blade hydrodynamic force along the ship advance direction $[N]$
F_Y	Blade hydrodynamic force perpendicular to the ship advance direction $[N]$
K_I	Integral parameter of PI control
K_P	Proportional parameter of PI control
l	Blade length $[m]$
N	Blades number
R	Cross-flow propeller radius $[m]$
Re	Reynolds number
V	Tank flow velocity $[m.s^{-1}]$
V_a	Ship advance speed $[m.s^{-1}]$
V_r	Rotational tip speed $[m.s^{-1}]$
W	Relative velocity $[m.s^{-1}]$

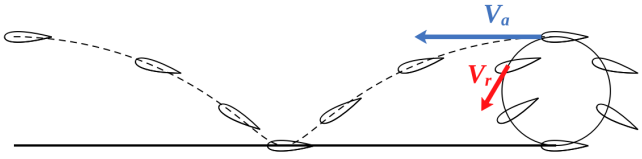

Figure 2: Illustration of the trochoidal path of one blade

Cross-flow propellers have been studied since the 20th century beginning by Kirsten (1922) with the dual scope of propeller and generator purposes with a fixed low-pitch mechanical system. Schneider (1928) improved on Kirsten's propeller and partnered with Voith in 1928 to industrialize and commercialize their propeller known as the Voith-Schneider Propeller (Bartels and Jürgens, 2006). Since, many experiments have been performed in Japan (Taniguchi, 1962), in North America (Bose and Lai, 1989; Ficken and Dickerson, 1969; Haberman and Harley, 1961; Nakonechny, 1974; Roesler et al., 2016), and in Netherlands (van Manen, 1966) to investigate this specific type of propulsion.
Meanwhile, theoretical models have emerged to handle the complex flow description and predict the performance of these systems. In 1962, Taniguchi (1962) developed a quasi-steady method to numerically estimate the performance of epicycloidal propellers (improved in 1981 by Zhu (1981)), Sparenberg and De Graaf (1969) proposed a theoretical model for a single-blade propeller by minimizing kinematic energy in the wake. Mendenhall and Spangler (1973) used a discrete-wake-vortex method to predict the behavior of a cycloidal propeller. Bose (1987) adapted a multiple-streamtube-model from wind turbine theory to study the high-pitch cycloidal propeller. Recent studies have implemented more complex models to estimate as well as possible cycloidal propeller performance (Epps et al., 2019; Halder et al., 2018). Lastly improvements on modern CFD solvers are accurate validation resources and a new interesting area of work for optimization purpose (Bakhtiari and Ghassemi, 2020; Esmailian et al., 2014; Fasse et al., 2019; Hu et al., 2020).

Cycloidal propellers blades have so far basically been actuated by mechanical rotating technology (connecting rods, crank, camshaft, gears...) and then restrained to only one kinematic mode (epicycloidal or trochoidal). While low-pitch systems provide high thrust at very low ship speed

(for harbour manoeuvring or dynamic positioning for example) they are limited in maximal ship speed (approximately 15knots for the Voith-Schneider Propeller). High-pitch systems can reach a higher ship speed but are less efficient during the starting phase.
To take advantage of both modes, the IRENav considered the design of an experimental cross-flow propeller with an electrical blade actuating. Three servo-motors reliant to the main rotation are imposing independent blade movements. Blade control is no longer limited by a mechanical system, all types of pitch law could be played. This allows pitch laws from both modes to be used and to switch from one mode to the other during the rotation of the propeller.
Another consideration is to play non-symmetric laws (from the two halves of rotation disk point of view). Indeed, as mentioned by Roesler et al. (2016), since downstream blades pass through the wakes of upstream blades, it is logical that optimal pitch law on the downstream half should be different from that on the upstream half. Physical phenomenon described by Halder et al. (2018) and resumed as dynamic virtual camber effects, lead also to view the two half disk domains different for the generation of hydrodynamic loads.
This experimental cross-flow propeller is also instrumented with a blade-embedded load-cell, a torque sensor and encoders to measure time dependant hydrodynamic loads and angles during the rotation. The goal of this paper is to present this experimental system from a mechanical aspect and its blade control/command. Several pitch laws from both kinematic modes are tested and pitch track-back is compared to the reference law. Then experimental setup and post-process are described. Lastly, preliminary measurements for several sinusoidal pitch laws are presented and discussed.

2. Experimental Propeller Design

The experimental cross-flow propeller presented here is an academic project driven by the French Naval Academy Institute in collaboration with IFREMER. The goal of this experimental blade-controlled platform is testing cycloidal systems pitch laws for design or optimization purpose. The platform also could generate measurements data for comparison or validation purpose. In this paper, the system is described as a propeller but it could also be used to test pitch law for marine energy converters (as it has originally been designed (Delafin et al., 2021; Paillard et al., 2015)).

2.1. Mechanical Description

The experimental blade-controlled platform is named SHIVA for Intelligent Hydrodynamic System with Angle Variation. Figure 3 gives a Computer Aided Design (CAD) rendering of SHIVA and the main characteristics in the table (bold values highlight those used for the configuration of the presented results). SHIVA is a large experimental system (800kg, 2.5m high) composed of a steel triangular frame [F] connected to the main vertical driveshaft by a Morse taper and rotating through the fixed outer frame [D]. This outer frame is built from steel I-beams which ensure stability during the experiments. On the triangular frame three vertical shafts are assembled by sliding link to be able to move them far or toward the triangular frame center. These sliding guides are 7°-tilted to allow for an axisymmetric system, and to be able to double the diameter to greatly modify the system's solidity (for present experiments the smallest diameter is chosen, D=0.8m). The radius of the propeller is defined as the distance between the center of the triangular frame and the center of each vertical secondary shaft. Three blades [I] are hooked up to each shaft and secured by bolts. Blades are made with filled stainless steel on a NACA0018 profile of 0.15m chord and 1m span. Blades can be wrapped in epoxy-fiberglass shell to increase the chord length to 0.35m. These shells also allow the blade profile to be changed and thus also modify the solidity of SHIVA. The solidity for the present experiments is 2.62.
The triangular frame is driven by the 2.5kW HRS115E6-130S (from SEM brand) main motor located at the top of the propeller [A]. A 50-ratio speed reducer [C] is used to increase the nominal torque and fit the rotational speed for our experiment values ($\sim$ 0-50 RPM). Each blade is also independently actuated by a 0.8kW HDM105C10-54S (from SEM brand) auxiliary motor [E]. A 10-ratio speed reducer is also used to adapt the motor rotational speed to the blade kinematic. The blades rotate around the quarter of their chord, close to the hydrodynamic center for the NACA0018 profile.
This blade rotation is commonly called pitch angle and pitch law refers to the function of this pitch angle along the orbital position θ. This pitch angle could be represented in two equivalent ways:

- φ which is the oriented angle between the advance speed direction (X- direction) and the blade chord line
- β which is the oriented angle between the ortho-radial line and the blade chord line

These two pitch angles are linked by the relation $\theta=\varphi-\beta$ (see Figure 4).
As illustrated in the introduction of the paper, for trochoidal mode, because the ship speed V_a (equal in this study to the tank flow speed V) prevails, the blade's leading edge is always aligned with the advance speed direction. Therefore φ oscillates around 0° (depending on the pitch law) and θ always increases while $\beta=\varphi-\theta$ always decreases during the main rotation. Under epicycloidal mode, the rotational tip speed V_r prevails so the blade's leading edge is aligned with the tangent of the rotation. Therefore β oscillates around 0° whereas φ is always increasing. Thus, for a simpler representation of the pitch law in figures, φ is used in case of trochoidal motions and β is used for epicycloidal motions.

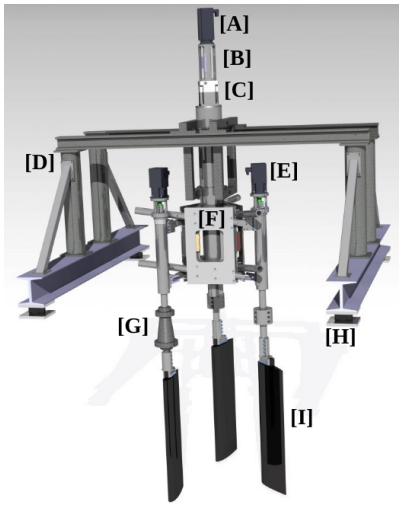

[A] Main Engine	Nominal Speed Ω_{main} Nominal Power P_{main}	3000 [RPM] 2500 [W]
[B] Torque Sensor	Measuring Range and Uncertainty (% of range)	$\pm$20 [$N.m$] ; 0.5%
[C] Speed Reducer	Ratio	50
[D] Outer Frame	Total Weight	1000 [kg]
[E] Auxiliary Engines with Speed Reducer	Nominal Speed Ω_{aux} Nominal Power P_{aux} Ratio	1800 [RPM] 790 [W] 10
[F] Triangular Frame	Diameter ($D = 2R$) Solidity ($\sigma = Nc/R$)	**0.8** – 1.6 [m] 0.5625 – 1.12/1.3 – **2.62**
[G] Blade load-cell	Measuring Range and Uncertainty	$F_{Nb} \pm 5000$ [N] ; 0.81% $F_{Tb} \pm 1000$ [N] ; 1.76%
[H] Fixed load-cells	Measuring Range and Uncertainty	F_x ± 5000 [N] ; 0.8% $F_y \pm 5000$ [N] ; 0.22% F_z 7000 [N] ; 0.54%
[I] Blades	Number of blades N Blade chord (c) Aspect Ratio ($AR = l/c$) Chord ratio ($c_r = c/R$) Blades cross section	3 0.15/**0.35** [m] 6.7/**2.8** 0.19 – 0.38/0.44 – **0.87** NACA 0018

Figure 3: On the left is a CAD view of SHIVA and on the right is the table of characteristics (for sensors, percents are giving the uncertainty of the measure)

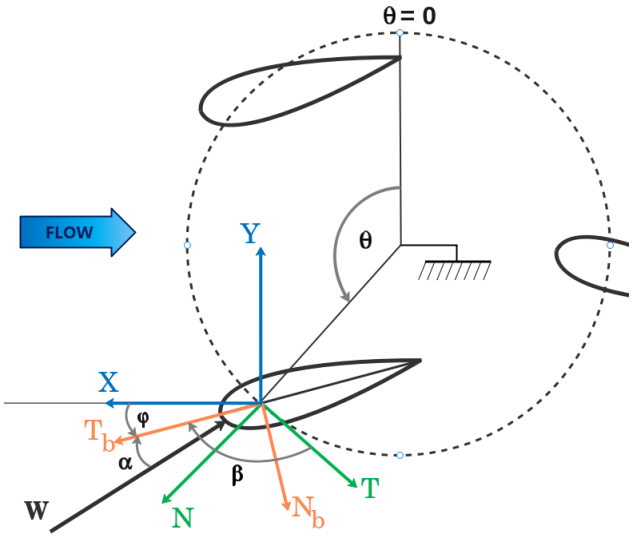

Figure 4: Representation of angles for an arbitrary position θ and an arbitrary relative velocity W

The pitch is directly related to the incidence α which is the angle between the blade chord and the local relative velocity W equal to the vectorial sum of the tank flow speed and the rotational tip speed. Indeed, for cross-flow propellers, the aim is to orientate the blade during the rotation with the pitch angle in order to maximize the contribution of lift and drag forces, generated by the incidence α, that produces a thrust in the advance direction (X direction in this case). The pitch angle has a major impact on cross-flow propeller design because it also influences back hydrodynamic loads by affecting the flow incidence with the induced pitch velocity.

To carry out experiments, SHIVA operates at the IFREMER wave and current flume tank which is 18 meters long by 4 meters wide and 2 meters deep (see Figure 5). The dimensions of SHIVA are suited to reduce the hydrodynamic blockage effect. Indeed the ratio of the propeller frontal area divided by the tank section leads to a blockage ratio of 15%. According to a previous study (Consul et al., 2013), the blockage effect overestimates hydrodynamic loads and efficiency for a ratio up to 50%. Here, these effects are thus neglected.

The fixed outer frame relies on two additional horizontal I-beams which elevate the whole system just above the water: only the blades are under the water line of the tank (see Figure 3 and Figure 5). An alignment of the outer frame with the water tank guarantees that the flow direction is parallel to the outer frame. A mechanical adjustment of the 0°-position of the main rotation (corresponding to the triangular frame) and 0°-positions β_i of the three secondary motors are also done before every experiment to ensure that the incoming flow is also parallel to each 0°-position β_i pitch blades (no incidence angle) for theta 0°-position. The flow velocity V is adjustable from 0.1 to 2.2 m/s, with a turbulence intensity of 1.5 %. Further information about IFREMER tank facilities are given by Gaurier et al. (2013) and Ikhennicheu et al. (2019).

For this study, the flow velocity is set at 0.8 m/s and 1.2 m/s and the main rotation Ω is limited to 50 RPM to avoid any risks of damage considering the important rotating payload. For these velocities, fiberglass-epoxy shells have been added to increase blade chord length and thus better suit the hydrodynamic forces level to the load-cell measuring ranges (detailed in the next section).

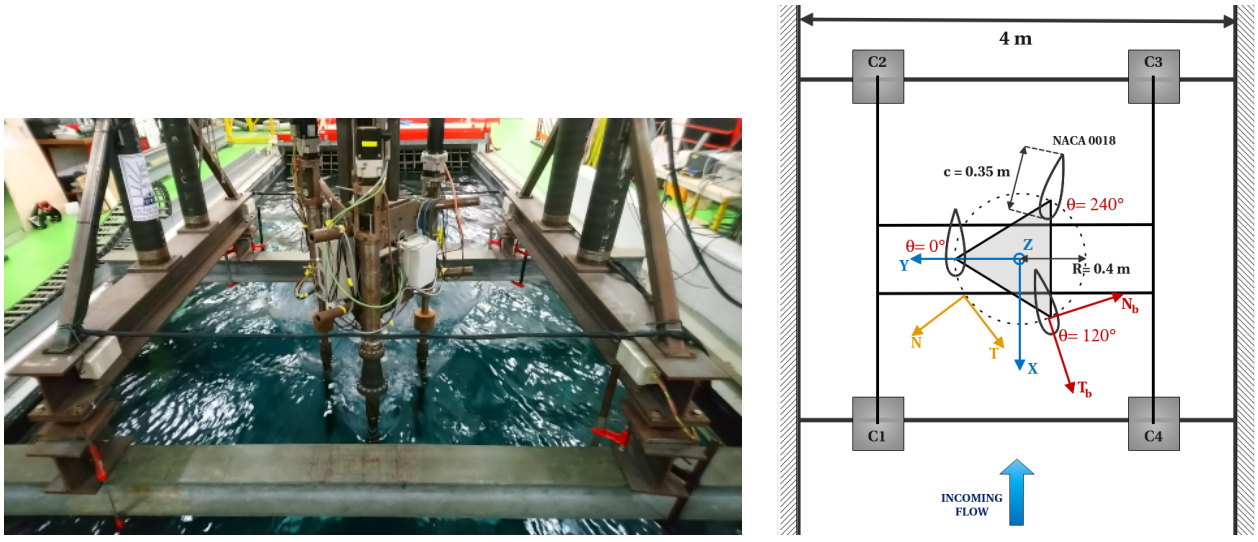

Figure 5: SHIVA overview at the IFREMER wave and current flume tank

2.2. Measurement Instrumentation

SHIVA is instrumented with 4 fixed 3-components load-cells [H] located between the outer frame and the tank I-beams (noted C1 to C4 in Figure 5). These load-cells provide global resulting solicitations of the propeller acting on the frame in the three directions **X**, **Y** and **Z** (see Figure 5). They measure loads for a range of $\pm 5000N$ in the X and Y direction and $+7000N$ in the Z direction (compression). Transfer matrix and uncertainty are given by the supplier (Six-axes) and resumed in the table of Figure 3.

One blade is instrumented with a 4-component load-cell [G] which measures local hydrodynamic loads in the direction of blade's chord **Tb** and normal to the blade **Nb** (see Figure 5). In-house calibration procedure was undertaken to determine matrix transfer to optimally reproduce the way the blade is stressed during experiments.

A torque sensor (4503B 020 L P0 00 KA2 from Kistler brand) is installed between the main motor and the main speed reducer [B] and measures the torque applied on the main driveshaft with a measuring range between 0 and 20 N.m and an uncertainty of 0.5% of the measuring range.

A CompactDAQ system from National Instruments (embedded NI cDaq-9184 linked with the stationary NI cDaq-9185) collects and synchronizes the data from all these measurement devices (embedded and fixed).

During the rotation, the pitch angles β_i of each blade and orbital position θ are also recorded thanks to incremental rotary encoders with a 1024 pulse rate (8.KIS40.1362.1024 from Kübler brand) to provide both the real angle values (for projection of local forces into the global reference frame) and feedback for the pitch control which is detailed in the next section. These encoders rotate with pulley-belt systems. According to the ratio of pulley transmission (25 for the principal axis and 4 for secondary axis) the resulted angle precision is 0.017° for θ and 0.088° for β. Due to the belt strain, an approximate error of 0.2° is estimated for β angle (for θ angle, the belt is always tightened because SHIVA always rotates in the same direction).

A 12-channel slip ring is used to transfer measurement signals from the blade load-cell to the triangular frame and an other 32-channel slip ring is used to transfer signals and power of embedded devices from rotating triangular frame to the outer frame and vice versa.

A Labview code allows users to synchronize collected measurements and set the parameters to capture data as sampling time and duration of acquisition.

2.3. Electrical Description

2.3.1. Macro Overview

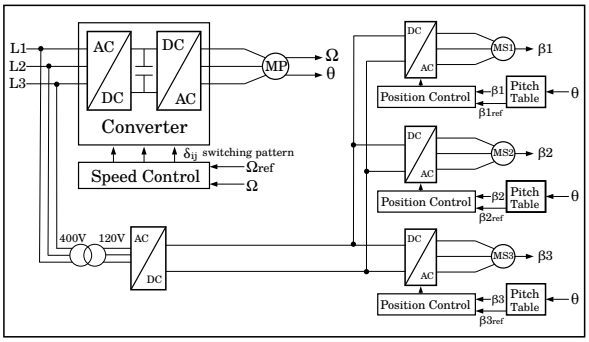

Figure 6: Electrical Diagram of the command architecture

The particularity of SHIVA lies on its electrical blade-control system which allows a wide range of pitch law investigation. As mentioned previously, SHIVA is composed of four permanent magnet synchronous machines (PMSM) (see Figure 6), one for the main rotation and one for each blade. The main PMSM (MP), which provides the rotational

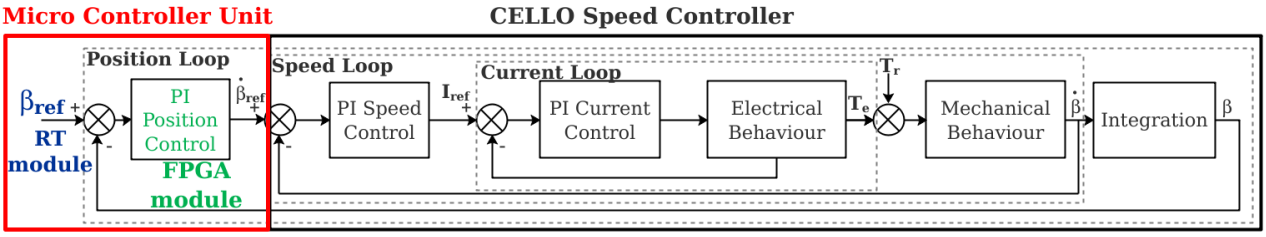

Figure 7: Diagram of Position Loop Control

speed, is alimented by a back to back converter powered by the 400V Alternative Current network. The MP speed is controlled by a servo drive controller, TUBA series from Elmo brand (TUBA12/460R), which regulates the speed Ω of the MP with regard to the reference speed Ω_{ref}. The speed control is carried out by two Proportional-Integral (PI) controller strategies (one for the speed Ω and one for the current) which are used by default for the TUBA servo drive controller.

This main axis is supervised by a LabVIEW code through a Computer-Human Interface (CHI) which allows users to set the reference speed of SHIVA. This CHI communicates through a controller area network (CAN bus) with the TUBA, which is installed in an electrical cabinet alongside the IFREMER tank, and the MP at the top of SHIVA.

Another network 120V Direct Current is created through a transformer and a rectifier also installed inside the electrical cabinet from the 400V AC (see Figure 6). Then this network powers the three secondary PMSM (MS1, MS2, MS3) which rotates the blades through an embedded inverter for each secondary axis (the main slip ring is used to transfer power from the electrical cabinet to SHIVA). MSi are controlled in position by digital servo drives, CELLO series from Elmo brand (CEL-A15/200R). Three PI controllers for each MSi are used: one for current, one for pitch rate $\dot{\beta}_i$ and one for pitch angle β_i. The way the blade-control is computerized uses the β angle, rotation of the blade in regards to the ortho-radial tangent. The pitch reference $\beta_{i_{ref}}$ is tabulated in function of the orbital position θ_i of each secondary axis. One of the special capacities of SHIVA is that each blade can follow a particular pitch law that procures a wide flexibility and range of investigation. Thanks to a second CHI, these pitch laws can be loaded even during the rotation.

2.3.2. *Specific Description of Blade-control*

Contrary to the main axis, the blade pitch control system is embedded in SHIVA. In-house tests and developments over the past two years have involved the installation of an embedded Micro-Controller Unit (MCU) to dramatically boost the responsiveness of the system in comparison with an external computer. This MCU, a CompactRIO system from National Instruments, is divided into two entities: a Real Time computer module (RT) which executes LabVIEW Real-Time applications and offers multi-rate control, execution tracing and communication with peripherals ; together with a user-programmable FPGA module which excels at smaller tasks that require high-speed logic and precise timing.

Figure 7 shows the classic blade-control diagram used for SHIVA. The position loop is executed into the MCU for each secondary axis and then speed and current loops are executed by CELLOs which are positioned on SHIVA. The advantage of moving the position control from the industrial CELLO to the MCU is to be able to modify PI parameters in real time to have accurate control under various kinematic conditions.

Pitch laws are tabulated into the RT which has a large memory space. For each blade-control iteration, pitch reference β_{ref} is given according to the blade orbital position θ. Because of the use of the embedded system, an incremental rotary encoder is mounted on the triangular frame to measure this orbital position of SHIVA during the rotation and to send the information directly to the MCU. Real pitch angle feedback, β, is also given by incremental rotary encoders mounted on each blade shaft. All these encoders are actuated by belt pulley system.

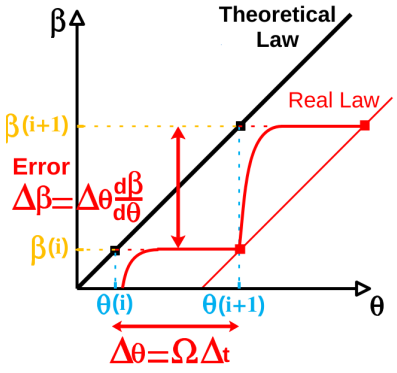

Figure 8: Schematic Error of Blade-control

The use of this PI controller strategy leads to a systematic error of pitch angle. Figure 8 illustrates this blade-control error for the case of a linear theoretical law (for example the case of the circular translation, β=$-\theta$, the blade is always parallel to the incoming flow). For each blade-control iteration, the controller will search in the tabulated law for the new reference pitch angle $\beta_{ref}(i)$ for the considered orbital position $\theta(i)$. And between two iterations, the blade holds this position until the new position. This causes a systematic

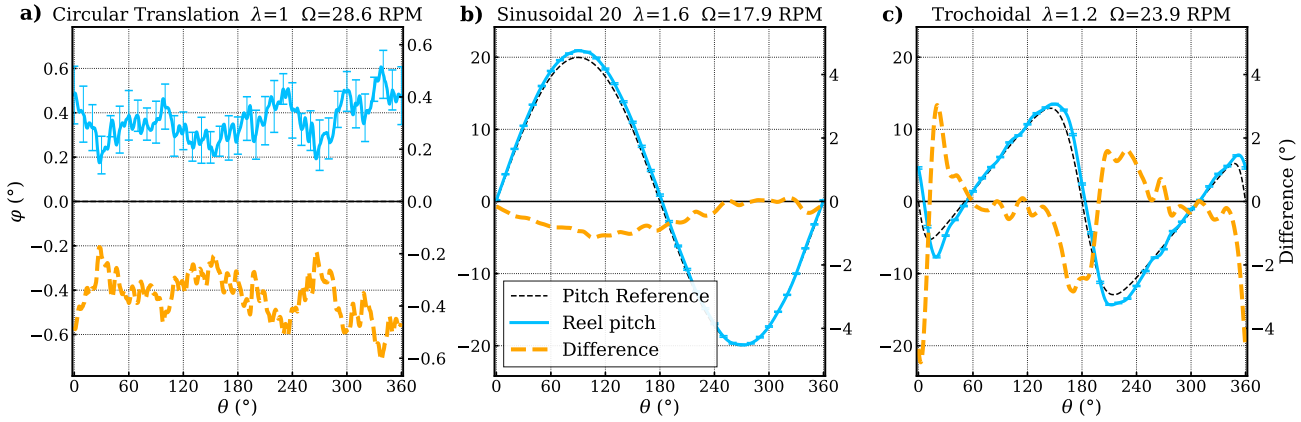

Figure 9: Pitch tracking in trochoidal mode for **a)** Circular Translation λ=1 pitch law; **b)** Sinusoidal 20deg λ=1.6 pitch law; **c)** Trochoidal λ=1.2 pitch law. Blade pitch angle φ on the left axis and difference between real and reference pitch on the right axis

delay of the real position $\Delta\beta = \beta(i+1)-\beta(i)$ which depends on:

- The complexity of the pitch law $\frac{d\beta}{d\theta}$: the sharper the derivative is and the higher the error
- The rotational speed Ω: the angular step $\Delta\theta$ between two iterations depends on Ω for a given time step
- The time step Δt: sampling time of the regulation loop (time between two iterations)

Figure 8 illustrates the error in the case of a linear pitch law (such as trochoidal mode, the blade rotates between 0° and 360° in order to keep the leading edge parallel to the incoming flow). For the case of a law in epicycloidal mode, the reference oscillates around β=0°. Hence the error fluctuates between delay or advance according to the derivative $d\beta/d\theta$ sign.
Because pitch laws are stored in the RT module, the regulation loop is limited by its sampling time which is around 2ms. The table below gives angular steps $\Delta\theta$ in function of rotational speed for Δt=2ms:

Ω (RPM)	10	20	30	40
$\Delta\theta$ (°)	0.12	0.24	0.36	0.48

Given the derivative ratio $d\beta/d\theta$ (which mostly depends on the orbital position) for an arbitrary pitch law and the rotational speed, this systematic error can be then estimated. Another delay of the real pitch control occurs when the pitch acceleration is higher than the capacities of auxiliary engines. In particular, for some pitch laws in epicycloidal mode (where the rotation is higher than trochoidal mode), acceleration limits of engines are reached at some period of the law. The next section illustrates these points by giving results of pitch tracking for various pitch laws under different kinematic conditions.

2.3.3. Pitch Tracking validation

The following results of pitch tracking have been computed from in-water measurements. The aim was to test various pitch laws for both kinematic cases, epicycloidal mode (λ<1) and trochoidal mode (λ>1). The flow velocity is set at 1.2 m/s for trochoidal laws and 0.8 m/s for epicycloidal laws and rotational speed is calculated to reach desired λ value.
Real pitch is recorded from rotary encoder and then phase-averaged over 30 rotation periods. The mean pitch is compared to the input reference law over one period. For trochoidal mode, φ pitch angle is shown instead of β angle for a simpler viewing.

Figure 9 shows pitch tracking for three trochoidal laws. The circular translation (Figure 9-a) is defined as the blade's leading edge is always parallel to the tank flow direction (i.e. φ=0 or β=-θ). For this law, the rotational speed is set at 28.6 RPM. A low constant delay is observed at just under 0.4° which is due to the systematic error shown previously. The real pitch is always delayed compared to the reference. The standard deviation shows a uniform distribution of the real pitch over orbital positions for all the different laps (here the pitch angle is close to 0 compared to other figures, this is why the deviation seems wide).
The sinusoidal pitch law with 20° amplitude (Figure 9-b) is well tracked with a satisfying maximal error under 1°. This maximal error occurs at the position θ=120° and is correlated to the manifestation of the highest measured hydrodynamic load. Indeed hydrodynamic forces involve pressure on blades that makes the reference law more difficult to follow. The standard deviation shows a low dispersion over the measurement laps.
The third pitch law (Figure 9-c) refers to a kinematic process of optimization in trochoidal mode used to boost the efficiency of the system for complex law (Hauville et al., 2018). This law presents some quick transitions which lead to an increasing tracking error (for θ between 340° and 20° and θ around 180°) but globally the blade closely follows the reference even if the rotational speed is higher than for the sinusoidal case.

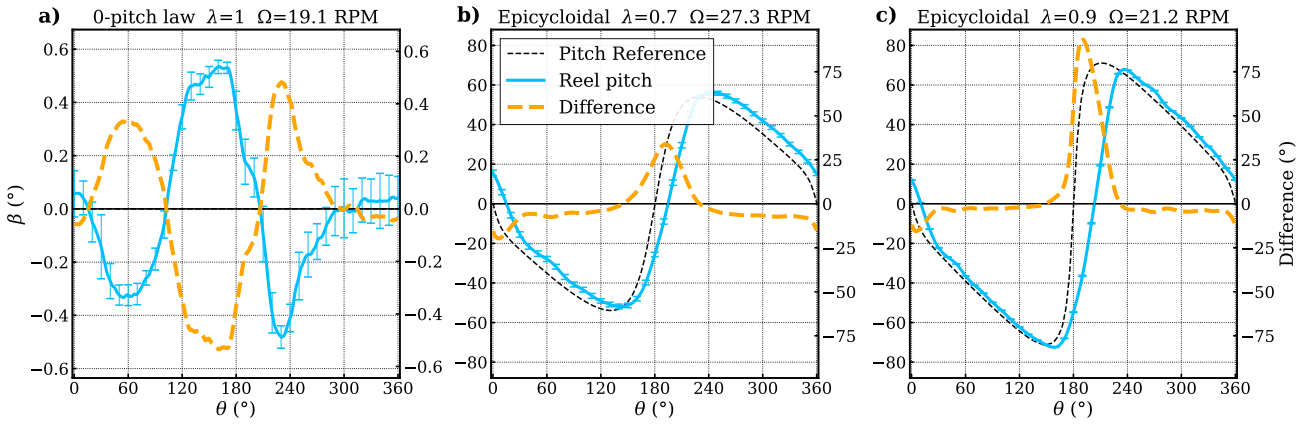

Figure 10: Pitch tracking in epicycloidal mode for **a)** 0-pitch law for λ=1; **b)** Epicycloidal λ=0.7 pitch law; **c)** Epicycloidal λ=0.9 pitch law. Blade pitch angle β on the left axis and difference between real and reference pitch on the right axis

Figure 10 shows pitch tracking results for epicycloidal mode. For the case of the 0-pitch law (Figure 10-a), the set-point is zero for all orbital positions: the blade stays parallel to the main rotor disk (it's the case for no-pitch systems such as Darrieus turbines in renewable marine energy domain). The blade follows the reference well with a maximal error of around 0.6°. This error oscillates around 0 because of the changeable relative flow direction over the orbital position. Again the standard deviation seems high here because of the closeness of the pitch law to 0, but it shows a uniform dispersion over orbital positions.

Figures 10-b and 10-c refer to two epicycloidal pitch laws which was again optimized by a kinematic process (Hauville et al., 2018). For these laws, the blades reversed at θ=180° (β switch from negative to positive value) that induces a high acceleration to servo-motors. The pitch tracking is thus less accurate during this blade reversal. The difference is even higher for the case of λ=0.9 pitch law because of the quicker reversal than for the λ=0.7 pitch law. Fortunately it is not during this reversal blade movement that the blade generates the higher hydrodynamic thrust.
In the case of λ=0.7 (Figure 10-b), the rotation speed is higher than in the case of λ=0.9 for the same flow speed (due to the definition of λ). This leads to a higher systematic error during the soft motion phases of the blade ($\theta \in$ [30:150] and [210:330]). For both cases, standard deviation shows again a good repeatability over measurement laps.

These results show an accurate blade pitch tracking for the trochoidal case whereas a higher tracking error is observed for the epicycloidal mode essentially due to the reversal blade phenomenon and higher rotational speed. Indeed the use of servo-motors for blade pitching allows the propeller to run various pitch laws but is also subject to the following main limitations:

- Servo-motors speed and acceleration limits involve restrictions on the pitch curve shape and the derivative $d\beta/d\theta$
- Blade control strategy which implies a systematic error that depends on the rotational speed Ω and the sampling time of regulation loop Δt

Nevertheless, the presence of rotary encoders provide the real pitch feedback for both real time tracking and post-process procedure. The control-CHI also allows users to adjust both PI parameters (K_I,K_P) in the position loop in order to adapt the reactivity of blade-control and thus reduce the tracking error.
To decrease the systematic error, ongoing developments are undertaken to reduce the sampling time of the regulation loop by saving reference pitch laws into the FPGA module which is sampled at 0.05 ms and hence reduce the orbital step $\Delta\theta$ between two regulation iterations for the same rotational speed. Moreover, PID control with Derivative term could also reduce this error but it is not available for our speed controllers and thus requires new investment.
Nevertheless, classical PID controller strategy is not the most suitable method for fluctuating pitch law. Here the industrial speed controllers (CELLO and TUBA) use this method of blade control but a new strategy using non linear controllers could be investigated, even though this area of work is out of scope for the moment.

3. Cross-flow propeller prototype efficiency

This last section presents results from in-water measurements for sinusoidal pitch laws with three different amplitudes in the trochoidal mode. Experimental setup and post-process are first presented then results are discussed.

3.1. Experimental setup and Post-process procedure

First, in-air measurements are used to eliminate the centrifugal effect from the embedded load-cell measurements and mechanical internal resistance on the main torque sensor.
Then measurements in the tank without flow velocity and

rotation are carried out to remove buoyancy effects and pre-stress of fixed load-cell. These static measurements are taken for a range of orbital positions ($\theta \in [0, 360, 30]$) and pitch angles ($\beta \in [0, 360, 30]$). Because the variation of voltages doesn't exceed 5% as shown in Figure 11, the mean value is calculated and subtracted from the in-flow measurements. This step is repeated everyday, only for orbital positions, to ensure any unexpected behaviour.

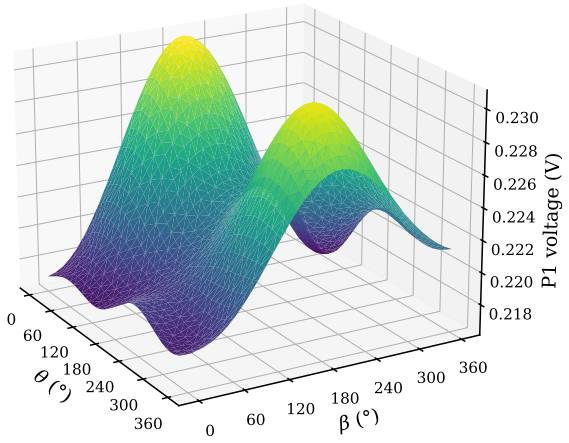

Figure 11: Representation of P1 Voltage of the embedded load-cell for the static measurements over 360° in θ and β

A mechanical verification of each blade position β_i and the position of the main axis θ is made before starting the flow motion to ensure that recorded angles correspond to the real motor position. In-flow measurements are launched after waiting for the flow to be well established at V=1.2m/s and the wake is stabilized with the rotational speed of SHIVA and the chosen pitch motion. K_I and K_P parameters are eventually adjusted to guarantee an accurate pitch tracking. Temporal signals are then recorded over 30 rotation periods. Because of the electromagnetic environment mainly caused by Pulse Width Modulation (PWM) of speed controllers, these temporal signals are disturbed by high frequencies. A low-pass filter (cut frequency of 30Hz) is applied on temporal signals.

Temporal voltages are then transformed to loads thanks to the transfer matrix. Pitch and orbital angles are used to convert local hydrodynamic loads from the embedded load-cell to global forces given by equations (2) and (3).

$$\begin{pmatrix} F_T \\ F_N \end{pmatrix} = \begin{pmatrix} \cos(\beta) & -\sin(\beta) \\ -\sin(\beta) & -\cos(\beta) \end{pmatrix} \begin{pmatrix} F_{Tb} \\ F_{Nb} \end{pmatrix} \tag{2}$$

$$\begin{pmatrix} F_X \\ F_Y \end{pmatrix} = \begin{pmatrix} \cos(\theta) & \sin(\theta) \\ -\sin(\theta) & \cos(\theta) \end{pmatrix} \begin{pmatrix} F_T \\ F_N \end{pmatrix} \tag{3}$$

All the loads are then phase-averaged over all the periods as shown in Figure 12. Means and standard deviations are calculated for each of the load signals.

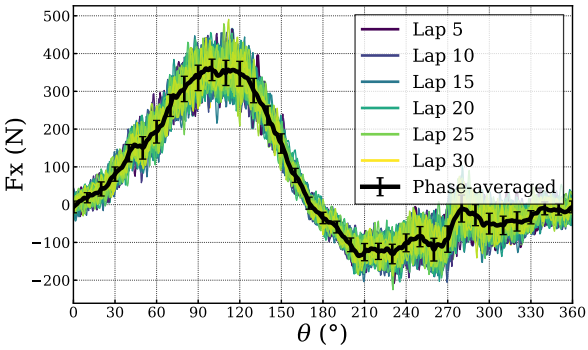

Figure 12: Phase-average operation over 30 periods for the Thrust signal in the case of the 20° sinusoidal pitch law for λ=1.2 and V=1.2m/s

Finally, as the embedded load-cell measures the hydrodynamic force on only one blade, mean-averaged loads are shifted of $\frac{\pi}{3}$ and $\frac{2\pi}{3}$ and added to construct the total hydrodynamic loads acting on all the three blades. By carrying out this operation, it is assumed that the whole blade has the same behaviour. The four fixed load-cells signals are also summed up to yield the total forces applied on the fixed frame.

Dimensionless force coefficients are given by following expressions:

$$C_F = \frac{F}{0.5\rho S V^2} \quad C_T = \frac{T}{0.5\rho S D V^2} \tag{4}$$

Where F is a hydrodynamic force and T a torque, S is the swept frontal area ($S = Dl$) and V the flume tank flow velocity.

Hydrodynamic efficiency is lastly defined as:

$$\eta = \frac{\overline{Fx_{tot}}\, V}{\overline{C_{tot}}\, \Omega} \tag{5}$$

Where $\overline{Fx_{tot}}$ and $\overline{C_{tot}}$ are respectively the mean of total Thrust and total Torque over 360°.

3.2. Sinusoidal pitch results

The post-process procedure is adopted on a 20° sinusoidal pitch law measurements at V=1.2 m/s and Ω=23.88 RPM (corresponding to λ=1.2), for which the mean local Reynolds number, $Re = \frac{cV}{\nu}$ is equal to 420 000. The Reynolds effect has not been taking into account in this study because the experimental set-up doesn't allow to carry out the Reynolds effect study (unable to reach Reynolds number up to 10^6).

Figure 13 gives single-blade force coefficients on the left and total reconstructed coefficients on the right. As shown on the polar plot, maximal thrust and side force are generated for θ between 90° and 120°. In the wake of the upstream blade, thrust tends toward zero and becomes even negative while side force reverses. The total reconstructed thrust is

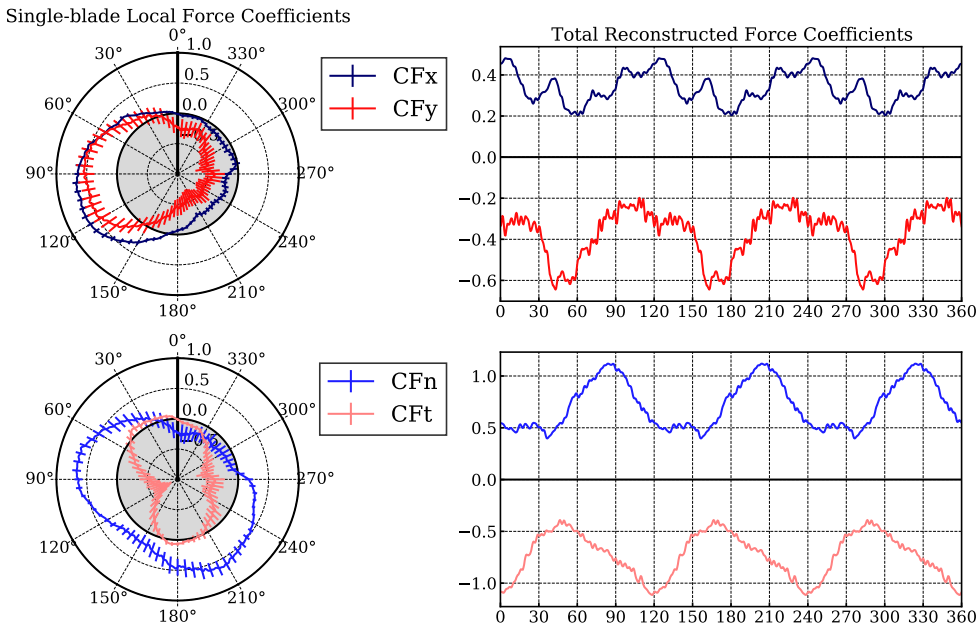

Figure 13: Single-blade Force coefficients at the left and Reconstructed total Force coefficients at the right for the case of the 20° sinusoidal pitch law for λ=1.2 and V=1.2m/s

always positive with some fluctuations while total side force is still negative, the wake is deflected on the tank side. This observation on the wake deflection is explained by the fact that for cycloidal propulsion the hydrodynamic center of thrust is not aligned with the rotor center.

For the normal and tangential coefficients, the distribution over orbital positions is quite different. Normal force is almost always spread outwards the rotor with two maximums at θ=70° and θ=210° while tangential force is almost always negative with two maximums at θ=120° and θ=270°. As the total tangential coefficient is still negative, this proves that generated hydrodynamic force counters the rotation of the main motor with fluctuations which can provoke damage. Therefore the propeller needs to provide a torque to generate the desired thrust.

Figure 14 presents the comparison between reconstructed force coefficients from the embedded load-cell and the measurements from fixed load-cells and the torque sensor. Mean values over 360° are represented by a short line at the left of each figure. Even if fixed sensors and embedded load-cell seem to measure the same global behaviour of the propeller, mean values over the period are slightly different. That implies a strong disparity with the hydrodynamic efficiency if it is expressed by fixed sensors or by embedded load-cell measurements.

These differences are mainly explained by the fact that embedded and fixed load-cells have a large measurement range (-5000N to 5000N) in comparison to measured hydrodynamic loads (-100N to 400N). For this reason, the flow velocity has been set at 1.2 m/s and blade chord has been increased with the addition of the epoxy-fiberglass shells to raise hydrodynamic loads.

This load increasing causes the frame to shake during the rotation of the propeller. This shaking is observed by a fixed load-cell as shown by large fluctuations on frame signals in Figure 14. It is also the case of the torque sensor which measures these oscillations on the main axis. But this shaking seems to be less detected on the instrumented blade which achieves a direct measurement of the flow whereas fixed load-cells measure loads which travel through all the mechanic parts of the platform. The embedded load-cell underestimates the total hydrodynamic loads. A new embedded load-cell with a smaller measuring range (±900N for normal blade direction and ± 400N for tangential blade direction) is currently manufactured to solve this problem.

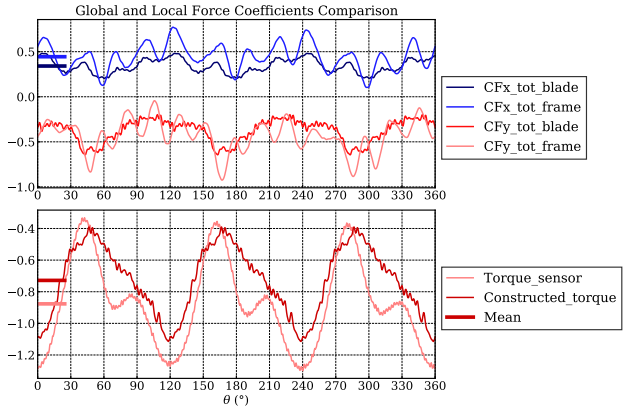

Figure 14: Comparison of blade reconstructed force coefficients and frame sensor force coefficients for the case of the 20° sinusoidal pitch law for λ=1.2 and V=1.2m/s

For the presented results, hydrodynamic efficiency is thus expressed using the mean of the total frame thrust divided by the mean of the torque sensor instead of the blade embedded load-cell measurements to take care in account the true solicitations of the experimental platform which are not detected by the embedded load-cell.
Measurements for other rotational speeds and other sinusoidal pitch laws are undertaken to determine the performance curve for sinusoidal pitch propeller. Figure 15 shows the results for the sinusoidal pitch laws of 10°, 20°, 30° and 40° of maximal amplitude.

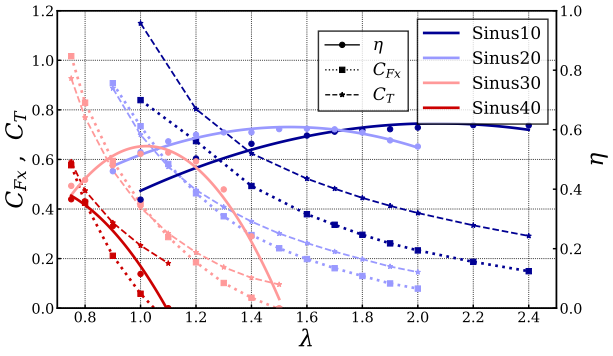

Figure 15: Efficiency and force coefficients versus advance parameter λ for 10°, 20°, 30°, 40° sinusoidal pitch laws

Results reveal that for the presented propeller configuration, the Sinus40 law has the lower hydrodynamic efficiency which falls when the advance parameter exceeds 0.8 value. This law isn't adapted to our configuration of solidity for an efficient purpose and for the trochoidal mode. Then, depending on the value of the advance parameter, each pitch law is interesting with a maximal efficiency reached for different values of λ. These results prove the need to adapt the pitch to the λ value. It also means that during the acceleration phase, it is preferable to start with high amplitude pitch law then decrease the pitch amplitude. Concerning the thrust, the Sinus10 law has the higher values for all the advance parameters. It shows that for manoeuvre which requires high thrust, the pitch must be decreased, balancing a reduction of the efficiency. Lastly, these results justify the use of vertical axis propeller with a variable pitch control system.
To go further, as perspective for next experiments, SHIVA will be used for experimental optimization purposes. Indeed, the complexity of the flow through the cross-flow propeller implies a strong discrepancy between upstream and downstream halves. Hence, there is no reason why the pitch law definition should be symmetrical (as in the case of most conventional cycloidal propeller). With a parameterization mehtod of pitch law which allows asymetrical curve (as referred by Abbaszadeh et al. (2019)), and a Gaussian Process method developed by Sacher et al. (2017), multiple-objective optimization could be done to determine the Pareto front through the dual objectives: maximizing the thrust and the efficiency. By repeating this process for many advance parameter values, optimal pitch laws will be established for various operation modes (low advance speed, cruising speed or transitional mode).

4. Conclusion and Perspectives

The experimental blade-controlled propeller designed at the Naval Academy Research Institute is presented in this study. Modular mechanical features allow comparisons for different solidity, Reynolds or aspect ratio numbers. The size of the system makes it ideal to test large-scale prototypes.
The technical progress published here is its electrical blade-control design which offers a huge range of pitch law investigations. Blade control/command is tested with in-house experiments comparing pitch reference and real pitch tracking. Even if the results reveal a suitable tracking, some limitations due to the technology of the speed controller are underlined. Indeed the use of regulation loop implies a systematic error which is hard to overcome. Using a more complex speed-control strategy could mitigate this error. Speed limitations of electric motors are also observed for high speed kinematics. As blade position angles are registered during the acquisition of measuring signals, this position error is acceptable for our investigations. However, a long-term upgrade of the control system is expected to improve the pitch tracking and the precision of angle measurements.
Post-process has been validated on sinusoidal pitch laws for trochoidal mode. Discrepancies on hydrodynamic measurements occurred between the blade embedded load cell and fixed load cells. These differences are mainly explained by a strong stress of the frame due to the high velocities encountered. Future experiments will be carried on with more precise load sensor measuring ranges, so that flume tank velocity and rotational speed could be reduced to be no more subject to high solicitations from the platform.
The results demonstrated here show the promising capacities of the platform in terms of propeller performance measurement. As a perspective in the quest for the ideal pitch law

and because the electrical blade-control system allows it, an experimental optimization procedure is intended for various advance parameter values.

5. Acknowledgements

This work was performed in the collaboration of the French Naval Academy and IFREMER. The constant support of the technical staff of the Naval Academy and IFREMER is warmly appreciated. Special thanks to Alain Boulch, Jean-Charles Kermabon, Arnaud Besle of Naval Academy, and Thomas Bacchetti and Jean-Valery Facq of IFREMER for the provided technical assistance.

References

Abbaszadeh, S., Hoerner, S., Maître, T., Leidhold, R., 2019. Experimental investigation of an optimised pitch control for a vertical-axis turbine. IET Renewable Power Generation 13, 3106–3112.

Bakhtiari, M., Ghassemi, H., 2020. Cfd data based neural network functions for predicting hydrodynamic performance of a low-pitch marine cycloidal propeller. Applied Ocean Research 94, 101981.

Barrett, D., Triantafyllou, M., Yue, D., Grosenbaugh, M., Wolfgang, M., 1999. Drag reduction in fish-like locomotion. Journal of Fluid Mechanics 392, 183–212.

Bartels, J.E., Jürgens, D., 2006. The voith schneider propeller: Current applications and new developments. Heidenheim: Voith Publication .

Bose, N., 1987. Rotary foil propellers. Tokyo, Japan: Ship Research Institute, Ministry of Transport .

Bose, N., Lai, P.S., 1989. Experimental performance of a trochoidal propeller with high-aspect-ratio blades. Marine Technology and SNAME News 26, 192–201.

Consul, C.A., Willden, R.H.J., McIntosh, S.C., 2013. Blockage effects on the hydrodynamic performance of a marine cross-flow turbine. Philosophical Transactions of the Royal Society A: Mathematical, Physical and Engineering Sciences 371, 20120299.

Delafin, P.L., Deniset, F., Astolfi, J.A., Hauville, F., 2021. Performance improvement of a darrieus tidal turbine with active variable pitch. Energies 14, 667.

Epps, B.P., Roesler, B.T., Medvitz, R.B., Choo, Y., McEntee, J., 2019. A viscous vortex lattice method for analysis of cross-flow propellers and turbines. Renewable Energy 143, 1035–1052.

Esmailian, E., Ghassemi, H., Heidari, S.A., 2014. Numerical investigation of the performance of voith schneider propulsion. American Journal of Marine Science 2, 58–62.

Fasse, G., Bayeul-Laine, A.C., Coutier-Delgosha, O., Curutchet, A., Paillard, B., Hauville, F., 2019. Numerical study of a sinusoidal transverse propeller, in: IOP Conference Series: Earth and Environmental Science, IOP Publishing. p. 052007.

Ficken, N.L., Dickerson, M.C., 1969. Experimental performance and steering characteristics of Cycloidal Propellers. volume 2983. Department of the Navy, Naval Ship Research and Development Center.

Gaurier, B., Davies, P., Deuff, A., Germain, G., 2013. Flume tank characterization of marine current turbine blade behaviour under current and wave loading. Renewable Energy 59, 1–12.

Haberman, W., Harley, E., 1961. Performance of Vertical Axis (Cycloidal) Propellers Calculated by Taniguchi's Method. Technical Report. David Taylor Model Basin Washington DC.

Halder, A., Walther, C., Benedict, M., 2018. Hydrodynamic modeling and experimental validation of a cycloidal propeller. Ocean Engineering 154, 94–105.

Hauville, F., Lecuyer-Le Bris, R., Deniset, F., Fasse, G., 2018. Pitch law optimization of a cycloidal propulsor, in: 16e Journees de l'Hydrodynamique, Marseille, France.

Hu, J., Li, T., Guo, C., 2020. Two-dimensional simulation of the hydrodynamic performance of a cycloidal propeller. Ocean Engineering 217, 107819.

Ikhennicheu, M., Germain, G., Druault, P., Gaurier, B., 2019. Experimental study of coherent flow structures past a wall-mounted square cylinder. Ocean Engineering 182, 137–146.

Kirsten, J., 1922. Propeller. US Patent 1432700. URL: https://patents.google.com/patent/US1432700.

van Manen, J.D., 1966. Results of systematic tests with vertical axis propellers. International Shipbuilding Progress 13, 382–398.

Mendenhall, M.R., Spangler, S.B., 1973. Theoretical Analysis of Cycloidal Propellers. Part II. Program Manual. Technical Report. Nielsen Engineering and Research Inc Mountain View California.

Nakonechny, B.V., 1974. Design of a 9-inch cycloidal propeller model unit and some experimental results. Technical Report.

Paillard, B., Astolfi, J.A., Hauville, F., 2015. Uranse simulation of an active variable-pitch cross-flow darrieus tidal turbine: Sinusoidal pitch function investigation. International Journal of Marine Energy 11, 9–26.

Roesler, B.T., Kawamura, M.L., Miller, E., Wilson, M., Brink-Roby, J., Clemmenson, E., Keller, M., Epps, B.P., 2016. Experimental performance of a novel trochoidal propeller. Journal of Ship Research 60, 48–60.

Sacher, M., Hauville, F., Duvigneau, R., Le Maître, O., Aubin, N., Durand, M., 2017. Efficient optimization procedure in non-linear fluid-structure interaction problem: Application to mainsail trimming in upwind conditions. Journal of Fluids and Structures 69, 209–231.

Schneider, E., 1928. Blade wheel. US Patent 1681500. URL: https://patents.google.com/patent/US1681500.

Sparenberg, J., 2002. Survey of the mathematical theory of fish locomotion. Journal of Engineering Mathematics 44, 395–448.

Sparenberg, J., De Graaf, R., 1969. On the optimum one-bladed cycloidal ship propeller. Journal of Engineering Mathematics 3, 1–20.

Taniguchi, K., 1962. Sea trial analysis of the vertical axis propellers. Mitsubishi Heavy Industries Ltd, Mitsubishi Technical Bulletin No. 6 .

Triantafyllou, M.S., Techet, A.H., Hover, F.S., 2004. Review of experimental work in biomimetic foils. IEEE Journal of Oceanic Engineering 29, 585–594.

Zhu, D., 1981. A computational method for cycloidal propellers. International Shipbuilding Progress 28, 102–111.